



저작자표시-비영리-변경금지 2.0 대한민국

이용자는 아래의 조건을 따르는 경우에 한하여 자유롭게

- 이 저작물을 복제, 배포, 전송, 전시, 공연 및 방송할 수 있습니다.

다음과 같은 조건을 따라야 합니다:



저작자표시. 귀하는 원 저작자를 표시하여야 합니다.



비영리. 귀하는 이 저작물을 영리 목적으로 이용할 수 없습니다.



변경금지. 귀하는 이 저작물을 개작, 변형 또는 가공할 수 없습니다.

- 귀하는, 이 저작물의 재이용이나 배포의 경우, 이 저작물에 적용된 이용허락조건을 명확하게 나타내어야 합니다.
- 저작권자로부터 별도의 허가를 받으면 이러한 조건들은 적용되지 않습니다.

저작권법에 따른 이용자의 권리와 책임은 위의 내용에 의하여 영향을 받지 않습니다.

이것은 [이용허락규약\(Legal Code\)](#)을 이해하기 쉽게 요약한 것입니다.

[Disclaimer](#)



工學碩士學位論文

**Fabrication of silver nanoparticles
decorated porous TiO₂ nanofibers for
highly efficient dye-sensitized solar cells**

은 나노입자가 부착된
다공성 이산화티타늄 나노섬유의 제조 및¹
고효율 염료감응태양전지로의 응용

2013年 8月

서울大學校 大學院

化學生物工學部

宋 喜

Abstract

Fabrication of silver nanoparticles decorated porous TiO₂ nanofibers for highly efficient dye-sensitized solar cells

Hee Song

School of Chemical and Biological Engineering

The Graduate School

Seoul National University

Silver nanoparticles decorated porous TiO₂ nanofibers (Ag/p_TiO₂ NFs) are used to enhance the performance of dye-sensitized solar cells (DSSCs). The Ag/p_TiO₂ NFs are fabricated *via* facile electrospinning method, etching process and chemical reduction. The porosity of the

porous TiO₂ nanofibers (p-TiO₂ NFs) is controlled by the amount of SiO₂ with electrospun TiO₂/SiO₂ composite NFs. The fabricated p-TiO₂ NFs exhibit high surface area, providing sufficient adsorption of dye on TiO₂. Moreover, surface plasmons from Ag/p-TiO₂ NFs enhance light absorption by trapping the incident light and increased the absorption of dye. In addition, DSSC composed of Ag/p-TiO₂ NFs demonstrate an optimized photovoltaic conversion efficiency of 8.8 %.

Keywords: Dye-sensitized solar cells, TiO₂ nanofibers, Ag nanoparticles, Surface plasmon

Student Number: 2011-24097

Contents

Chapter 1 Introduction	1
1.1 Dye-sensitized solar cells.....	1
1.2 One-dimensional nanomaterials.....	4
1.2.1 1-D nanostructured DSSCs	5
1.2.2 TiO ₂ nanofibers-based DSSCs	6
1.3 Metal nanoparticles.....	7
1.3.1 Plasmonic DSSCs	8
1.4 Objective of this study	9
Chapter 2 Experimental.....	11
2.1 Preparation of porous TiO ₂ nanofibers	11
2.1.1 SiO ₂ nanoparticles.....	11
2.1.2 Porous TiO ₂ nanofibers	12
2.2 Synthesis of Ag NPs decorated porous TiO ₂ NFs.....	13
2.2.1 Fabrication of silver NPs on porous TiO ₂ NFs.....	13

2.2.2	Protecting layer	14
2.3	Solar cell preparation	15
2.4	Characterization	16
Chapter 3 Results and discussion.....		19
3.1	Porous TiO ₂ nanofibers for solar cell application.....	19
3.1.1	Fabrication of porous TiO ₂ NFs.....	19
3.1.2	Characterization of porous TiO ₂ NFs.....	20
3.1.3	Surface area analysis of porous TiO ₂ NFs.....	26
3.1.4	Solar cell performance	31
3.2	Ag NPs decorated porous TiO ₂ NFs for solar cell application	35
3.2.1	Mechanism of Ag NPs in reduction process	35
3.2.2	Characterization of Ag NPs decorated porous TiO ₂ NFs	36
3.2.3	Optical property analysis	41
3.2.4	Solar cell performance	47
Chapter 4 Conclusion		51

List of Figures

Figure 1.	Energy level diagram showing the operation of the dye-sensitized nanocrystalline solar cell	3
Figure 2.	FE-SEM images of a) SiO ₂ /TiO ₂ composite NFs and porous TiO ₂ NFs b) TEOS 1 %, c) TEOS 1.5 %, d) TEOS 2 %. TEM images of e) SiO ₂ /TiO ₂ composite NF and f) porous TiO ₂ NF.....	23
Figure 3.	SEM/energy dispersive X-ray spectroscopy (SEM/EDX) spectra SiO ₂ /TiO ₂ composite NFs (before etching) a) TEOS 1 %, c) TEOS 1.5 %, e) TEOS 2 % and porous TiO ₂ NFs (after etching) b) TEOS 1 %, d) TEOS 1.5 %, f) TEOS 2 %.....	24
Figure 4.	XRD patterns for pure TiO ₂ NFs (black) and porous TiO ₂ NFs with TEOS 1 % (red), TEOS 1.5 % (blue), TEOS 2 % (violet).	25
Figure 5.	Nitrogen adsorption isotherms of a) pure TiO ₂ NFs and porous TiO ₂ NFs b) TEOS 1 %, c) TEOS 1.5 %, d) TEOS 2 %.....	28

Figure 6. Absorption spectra of N719 in NaOH mixed solution (water/ethanol = 1:1, v/v) desorbed from photoelectrode based on pure TiO ₂ NFs (black) and porous TiO ₂ NFs with TEOS 1 % (red), TEOS 1.5 % (blue), TEOS 2 % (violet)..	29
Figure 7. <i>J-V</i> characteristics of DSSCs prepared with pure TiO ₂ NFs (black) and porous TiO ₂ NFs with TEOS 1 % (red), TEOS 1.5 % (blue), TEOS 2 % (violet).....	33
Figure 8. TEM images of a) Ag/p_TiO ₂ NFs and b), c) Ag/p_TiO ₂ NFs with SiO ₂ protecting layer.....	38
Figure 9. Scanning transmission electron microscopy/energy dispersive X-ray (STEM-EDX) dot mapping of Ag/p_TiO ₂ NFs with SiO ₂ protecting layer	39
Figure 10. XRD patterns for a) porous TiO ₂ NFs and b) Ag/p_TiO ₂ NFs	40
Figure 11. a) Optical absorption spectra of porous TiO ₂ NFs (black) and Ag/p_TiO ₂ NFs (blue) in ethanol and b) difference of optical absorbance...	44
Figure 12. a) Optical absorption spectra of ruthenium dye molecules (red), p_TiO ₂ NFs with dye (black) and Ag/p_TiO ₂ NFs with dye (blue) in ethanol. b) Absorbance results from	

only dye are calculated in the following manner:

$$(\text{absorbance of NFs with dye}(\lambda)) - (\text{absorbance of NFs}(\lambda)).45$$

Figure 13. Absorption spectra of N719 in NaOH mixed solution
(water/ethanol = 1:1, v/v) desorbed from photoelectrode
based on porous TiO₂ NFs (black) and Ag NPs decorated
porous TiO₂ NFs with Ag 0.1wt % (red), Ag 0.2wt %
blue), Ag 0.3wt % (violet).....46

Figure 14. *J-V* characteristics of DSSCs prepared with porous TiO₂
NFs (black) and Ag NPs decorated porous TiO₂ NFs with
Ag 0.1wt % (red), Ag 0.2wt % (blue), Ag 0.3wt % (violet).

.....49

List of Tables

Table 1.	BET surface area and dye loading amount of pure TiO ₂ NFs and porous TiO ₂ NFs with increasing TEOS content..	30
Table 2.	Summary of the <i>J-V</i> characteristics of DSSCs prepared with various surface areas	34
Table 3.	Summary of the <i>J-V</i> characteristics of DSSCs prepared with different ratio of silver nanoparticles.	50

Chapter 1. Introduction

1.1 Dye-sensitized solar cells

Solar energy conversion by photoelectrochemical cells has been highlighted as eco-friendly and economically viable renewable energy sources. Especially, dye-sensitized solar cells (DSSCs) have attracted a great deal of interest in future solar cell markets because of their low fabrication cost and application to flexible and transparent solar cells [1-2].

DSSCs differs from the almost all other kinds of solar cells in that light absorption and charge carrier transport are each handled by different materials in the cell [3]. **Figure 1** displays energy level diagram showing the operation of the DSSC [4]. The photosensitizer, attached to a wide-band gap metal oxide such as TiO_2 , ZnO or SnO_2 ,

absorbs light and transfers the photoexcited electron to the conduction band of the semiconductor, which transport the electron to the collecting electrode [5]. The dye regenerated by electron transfer from a redox couple, usually comprised of iodide/triiodide (I^-/I_3^-) in organic solvent, which is then reduced at the platinized counter-electrode [6].

Up to now, the most efficient DSSC achieves power conversion efficiencies of 13 %, but the overall performance is still below the predicted values (31 %) [7]. Consequently, a large effort has been devoted to improve the efficiency by (1) searching new dye sensitizers for extending the light-harvesting region [8], (2) investigating the alternative electrolyte couples for lowering the redox potential to increase open-circuit voltage (V_{oc}) [7], (3) modifying the construction of the working electrode to either improve charge transport or enhance light absorption [9-10].

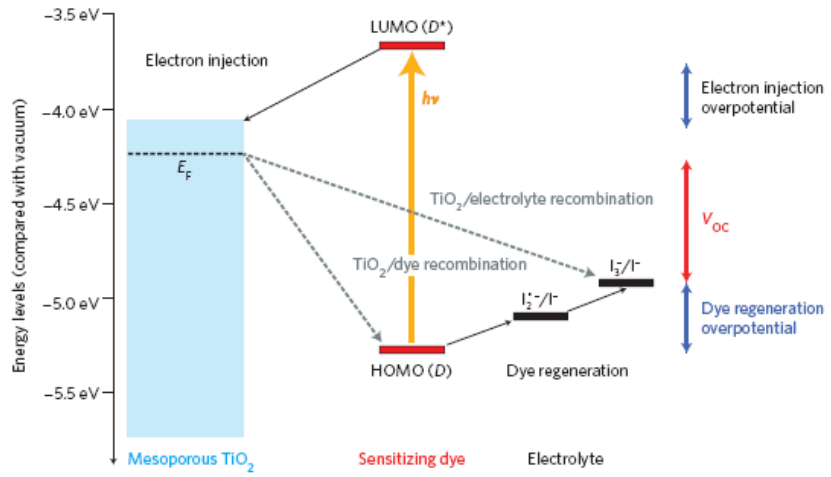


Figure 1. Energy level diagram showing the operation of the dye-sensitized nanocrystalline solar cell [4].

1.2 One-dimensional nanomaterials

One-dimensional (1-D) nanomaterials have been extensively studied in various applications such as electronic, photonic and electrochemical devices due to their thermal stability, mechanical property, optical property and electron transport property originated in dimensionality [11-13]. To date, a large number of fabrication techniques have been investigated for generating various morphological 1-D nanomaterials like fiber, wire, belt, rod and tube [14]. Of these fabrication methods, electrospinning is the most straightforward approach to nanofibers [15]. High voltage supply induces the surface charge of a polymer solution droplet. The electrostatic repulsions between the surface charges can overcome the surface tension of polymer solution and thus makes the ejection of a liquid jet through a spinneret [16].

1.2.1. 1-D nanostructured DSSCs

Among various routes to improve the DSSCs performance, rationalizing the morphology of the nanostructured photoanode is relatively simple and efficient way. To date, profound researchers have been developed novel shapes of photoelectrode such as hollow spheres, core-shell particles, tube and fibers [17-20]. The optimized construction of DSSCs enhanced power conversion efficiency mostly based on their increased surface areas to adsorb dye molecules and relatively large sizes for scattering incident light [21]. Particularly, the 1-D geometry at nanometer scale provides elongated direct pathways for electron travel leading to improved charge collection efficiency in DSSCs [22-23]. For this reason, there has been intensive research on fabrication of 1-D nanostructured photoanode with TiO₂ and ZnO during last decade.

1.2.2. TiO₂ nanofibers-based DSSCs

Titanium dioxide, chemical formula TiO₂, has been widely studied because of its adequate properties for pigment, photocatalyst and solar energy conversion [24-26]. TiO₂ is found to be rutile, anatase, and brookite forms in nature. Although rutile is the most thermodynamically stable form, anatase is preferred for DSSCs due to larger bandgap (3.2 vs. 3.0 eV for rutile) and higher conduction band edge energy, E_c [27]. Electrospun TiO₂ nanofibers (NFs) are one of the most attractive materials in the fabrication of DSSCs [28]. The use of TiO₂ NFs in DSSCs has great potential benefits such as fast electron transfer and reduced charge recombination based on 1-D structures or light scattering and enhanced light harvesting result from size effect [29-30]. However, TiO₂ NFs-based DSSCs showed limited performance because of insufficient dye adsorption owing to low surface area compared with TiO₂ nanoparticles-based DSSCs.

1.3 Metal nanoparticles

The importance of nanomaterials for areas ranging from physics, chemistry, engineering and even biology is significant [31-32].

Nanomaterials with enhanced physicochemical characteristics, such as high surface-to-volume ratio, quantum size effect and electrodynamic interactions, show unique and exceptional property compared to bulk materials [33-34].

Among various types of nanomaterials, metal nanoparticles, such as gold (Au), silver (Ag), and copper (Cu), attract tremendous attraction due to their unique optical, electronic and magnetic properties [35-36]. The optical properties of nano-sized noble metals are not merely reflecting light but strong visible-light absorption based on the interaction between metals and light in a field known as plasmonics [37]. Surface plasmons are collective oscillations of the free electrons

in metal nanoparticles at a specific surface plasmon resonance frequency [38]. Light can be trapped and concentrated due to surface plasmonic effect of metal nanoparticles [39]. Accordingly, these metal nanoparticles are widely used in electronic, catalysis, sensing and electrochemical application that involve light.

1.3.1. Plasmonic DSSCs

In the past few years, plasmonic metal nanoparticles have been applied to increase the optical absorption result in photocurrent enhancement in wide range solar cells because they can effectively trap the incident light inside the solar cells [40]. Especially DSSCs, these metal nanoparticles strongly scatter light and induce localized surface plasmons to enhance the electromagnetic field that also increases light absorption of dye molecules remarkably [41-42]. A strong surface plasmon at the desired resonance wavelength is

probably the most important factor in plasmonic DSSCs. The surface plasmon strength is proportional to the quality factor (Q):

$$Q = \frac{w(d\epsilon_r/dw)}{2(\epsilon_i)^2} \quad (1)$$

Where ϵ_r is real part of dielectric function, ϵ_i is imaginary part of dielectric function and w is the excitation frequency. Silver has the largest quality factor across the almost all spectrum from 300 to 1200 nm [43]. Hence, Ag nanoparticles have been widely utilized in a high-performance DSSCs due to their excellent qualities in terms of plasmonic ability, electrical conductivity and material cost.

1.4 Objective of this study

Herein, we report a fabrication of Ag nanoparticles decorated porous TiO₂ NFs (Ag/p_-TiO₂ NFs) for enhance the performance of DSSCs. Porous TiO₂ NFs (p_-TiO₂ NFs) with various surface area

were fabricated by a simple electrospinning and etching method with TiO₂/SiO₂ composite NFs. The porosity of the p-TiO₂ NFs was controlled by the amount of SiO₂ with electrospun TiO₂/SiO₂ composite NFs and adsorption of the sensitizers on TiO₂ NFs depends on the porosity. After the reduction of silver ions on TiO₂ NFs, surface plasmon effect of the Ag NPs was investigated by UV-Vis spectroscopy. Optical property of Ag/p-TiO₂ NFs and light absorption of dye molecules with Ag/p-TiO₂ NFs was compared to that of p-TiO₂ NFs. Additionally, p-TiO₂ NFs and Ag/p-TiO₂ NFs were applied to DSSCs to evaluate the improved photovoltaic properties.

Chapter 2. Experimental

2.1 Preparation of porous TiO₂ nanofibers

2.1.1. Fabrication of SiO₂ nanoparticles

Colloidal SiO₂ nanoparticles with an average diameter of 40 nm were prepared via Stöber method [44]. First of all, absolute ethanol (158 mL), ammonia solution (30 wt%, 7.8 mL) and deionized water (2.8 mL) were mixed at 50 °C for 30 min. Then 5.8 mL of tetraethyl orthosilicate (TEOS) was added to the solution and vigorously stirred for 12 h. After the reaction, the colloidal SiO₂ was isolated from the solution by centrifugation and washed twice with ethanol to remove residual reagents. The final product was re-dispersed in 100 mL of absolute ethanol.

2.1.2. Porous TiO₂ nanofibers

The 6 wt% of poly (vinyl pyrrolidone) (PVP, MW= 1,300,000) were dissolved in 5 mL of colloidal SiO₂ solution. Another solution containing 2 mL of titanium isopropoxide (TTIP), 2.5 mL of acetic acid and various TEOS concentration (1, 1.5 and 2%) were prepared followed by addition to the viscous colloidal SiO₂ solution. After the solution was evenly mixed, viscous precursor solution was injected into a 15 mL syringe. In the electrospinning process, the solution was fed through the spinneret (a metallic needle) that was connected to a direct current (DC) power supply. The syringe pump controlled the flow rate of solution for 10 µL min⁻¹. A 12 kV of voltage was supplied between the needle and the metal collector, which was grounded and used to collect NFs. The SiO₂/TiO₂ composite NFs were obtained after calcining the electrospun NFs at 500 °C for 6 h. To fabricate porous TiO₂ NFs, the SiO₂ portion of the SiO₂/TiO₂

composite NFs was etched with an HF solution which concentration was 1.7 wt% for 14 h. After etching process, porous TiO₂ NFs washed with excess deionized water to remove residual acid.

2.2 Synthesis of Ag NPs decorated porous TiO₂ NFs

2.2.1. Fabrication of silver NPs on porous TiO₂ NFs

At first, 100 mg of porous TiO₂ NFs was dispersed in 5 mL of ethanol. Then 50 μL ammonium hydroxide and 20 μL of (3-Mercaptopropyl)trimethoxysilane (MPTS) were added to the porous TiO₂ NFs dispersion and the resulting solution was stirred at room temperature for 12 h. After washing, MPTS-treated porous TiO₂ NFs were obtained and dried in a vacuum oven. MPTS-treated porous TiO₂ NFs (100 mg) were dispersed in 100 mL of ethylene glycol. Then, 10 mg of silver nitrate (AgNO₃) and 10 μL of

octylamine were introduced to the suspension of MPTS-treated porous TiO₂ NFs and the reduction of silver proceeded for 1 h on the MPTS-treated porous TiO₂ NFs at 25 °C with stirring. The resulting yellow product was obtained by centrifugal precipitation and washed several times to remove impurities.

2.2.2. Protecting layer

To prevent corrosion of Ag NPs by electrolyte, thin SiO₂ shell was introduced as a protecting layer. Ag NPs decorated porous TiO₂ NFs (100 mg) were dispersed in 30 mL of water and were stirred with PVP (MW= 40,000, 0.1 g) for 3 h. After the adsorption of PVP, Ag NPs decorated porous TiO₂ NFs were centrifuged and washed with water and ethanol and re-dispersed in 13.17 mL of absolute ethanol. The dispersion was mixed with 0.65 mL of ammonium hydroxide and 0.23 mL of water. Then, 50 µL of TEOS was rapidly injected to

the solution and stirred for 4 h at 35 °C. The final product was obtained after centrifugation, washing and drying in a vacuum oven.

2.3 Solar cell fabrication

Ag NPs decorated porous TiO₂ NFs, porous TiO₂ NFs and TiO₂ NFs were mixed with paste based on ethyl cellulose, lauric acid and terpineol. The resulting paste was deposited on fluorine-doped tin oxide (FTO) glass, which was pretreated with TiCl₄ and heated at 450 °C for 30 min, by screen-printing. The film was dried at room temperature and annealed by the same heating method used previously. The prepared electrode films were immersed into a solution of absolute ethanol containing 0.5 mM of N719 (Solaronix) for 36 h to assure complete sensitizer uptake. After washing with anhydrous ethanol for several times, the dye-sensitized electrode

was assembled with platinum-coated counter electrode using 60 μm -thick surlyn (Dupont). Then the sealed cell was filled with liquid electrolyte composed of 0.6 M 1, 2-dimethyl-3-propylimidazolium iodide (DMII), 0.1 M LiI, 0.05 M I_2 and 0.5 M 4-tert-butylpyridine in acetonitrile. In order to estimate the dye loading amount of photoelectrode, the dye was desorbed into 0.1M NaOH mixed solution (water/ethanol = 1:1, v/v). The amounts of dye were obtained from the measured the UV-Vis absorption spectrum of the resultant solution and the calibrated absorption coefficient, 1.41×10^4 $\text{M}^{-1} \text{ cm}^{-1}$ at 515 nm according to Beers' law.

2.4 Characterization

The morphology observation of Ag NPs decorated porous TiO_2 NFs, porous TiO_2 NFs and TiO_2 NFs was performed by field-emission

scanning electron microscopy (FE-SEM, JEOL 6700) and transmission electron microscopy (TEM, JEOL JEM-200CX). Energy dispersive X-ray spectroscopy (EDX) analysis data was obtained using a JEOL JSM-6700F. The scanning transmission electron microscopy/energy dispersive X-ray (STEM-EDX) dot mapping data was obtained using a JEOL JEM-2100F. X-ray diffraction (XRD) patterns were taken by M18XHF-SRA (Mac Science Co.) with a Cu K α irradiation at a scan rate (2θ) of 4° min^{-1} . Ultraviolet-visible (UV–Vis) spectra were acquired using a Lambda-35 spectrometer (PerkinElmer, USA). To obtain UV–Vis spectra, the samples were dispersed in absolute ethanol. Brunauer–Emmett–Teller (BET) nitrogen sorption experiments were conducted to calculate surface area using an ASAP 2010 (Micromeritics, USA). The photocurrent-voltage (I-V) properties of the DSSCs were measured using a 500 W xenon lamp (XIL model 05A50KS source units). The incident photon-to-current efficiency (IPCE, PV measurements, Inc.) spectra were measured as a function of wavelength from 300 nm to

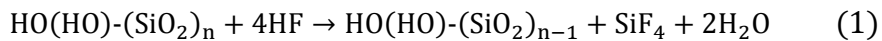
800 nm under short circuit conditions.

Chapter 3. Results and discussion

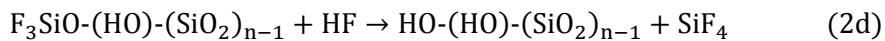
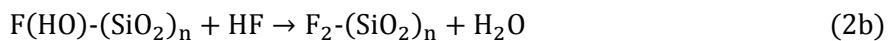
3.1 Porous TiO₂ nanofibers for solar cell application

3.1.1 Fabrication of Porous TiO₂ NFs

To fabricate porous TiO₂ NFs, the SiO₂ portion of the SiO₂/TiO₂ composite NFs was etched with an HF solution by the following chemical reaction equation.



The four sequential steps are concluded to be the essential one-cycle for SiO₂ etching.



In every step, the Si-O bonds are preferentially attacked by HF due to the Coulomb attraction between the polarized charges. The transition state appears with the formation of a four-member ring of Si-O-H-F. Subsequently, the reaction proceeds to the dissociation of Si-O and H-F bonds and the generation of Si-F and O-H bonds. In the first and second steps, the terminated OH groups are replaced by F atoms, and H₂O molecules are produced. The third step prominently contributes to the breaking of the SiO₂ network and the SiF₄ molecule finally detaches from the surface. Consequently, the silica part of the NFs was removed by HF treatment [45].

3.1.2 Characterization of Porous TiO₂ NFs

Figure 2 displays field-emission scanning electron microscopy (FE-SEM) and transmission electron microscopy (TEM) images of the SiO₂/TiO₂ composite NFs and porous TiO₂ NFs. As can be seen

in the SEM images, porous TiO_2 NFs were shorter than the $\text{SiO}_2/\text{TiO}_2$ composite NFs due to HF etching. Additionally, porous TiO_2 NFs were more divided as the SiO_2 portion (amount of TEOS in spinning solution) of the $\text{SiO}_2/\text{TiO}_2$ composite NFs increased. TEM image clearly shows pores of porous TiO_2 NFs after the removal of SiO_2 via HF etching.

SEM/energy dispersive X-ray spectroscopy (SEM/EDX) spectra exhibit successfully etching of SiO_2 (**Figure 3**). The atomic ratio between Si and Ti is 13 : 87 for $\text{SiO}_2/\text{TiO}_2$ composite NFs (TEOS 1%), 13.5 : 86.5 for $\text{SiO}_2/\text{TiO}_2$ composite NFs (TEOS 1.5%) and 14.5 : 85.5 for $\text{SiO}_2/\text{TiO}_2$ composite NFs (TEOS 2%). After the etching process, the atomic ratio of NFs is altered to for 1 : 99 for porous TiO_2 NFs (TEOS 1%), 1.4 : 98.6 for porous TiO_2 NFs (TEOS 1.5%) and 1.6 : 98.4 for porous TiO_2 NFs (TEOS 2%).

Figure 4 shows the X-ray diffraction (XRD) patterns of pure TiO₂ NFs and porous TiO₂ NFs. The characteristic diffraction peaks of NFs correspond to the anatase phase and agree well with the standard reported values (JCPDS No. 21-1272). Especially, the strong diffraction peak at $2\theta = 25.3^\circ$ (101) coincide with the peak of anatase TiO₂. Interestingly, a small peak at $2\theta = 31^\circ$ corresponding to the (110) peak of TiOF₂ was also detected for porous TiO₂ NFs. It has been reported that TiOF₂ can be formed by HF-etching the SiO₂/TiO₂ nanocomposite [46].

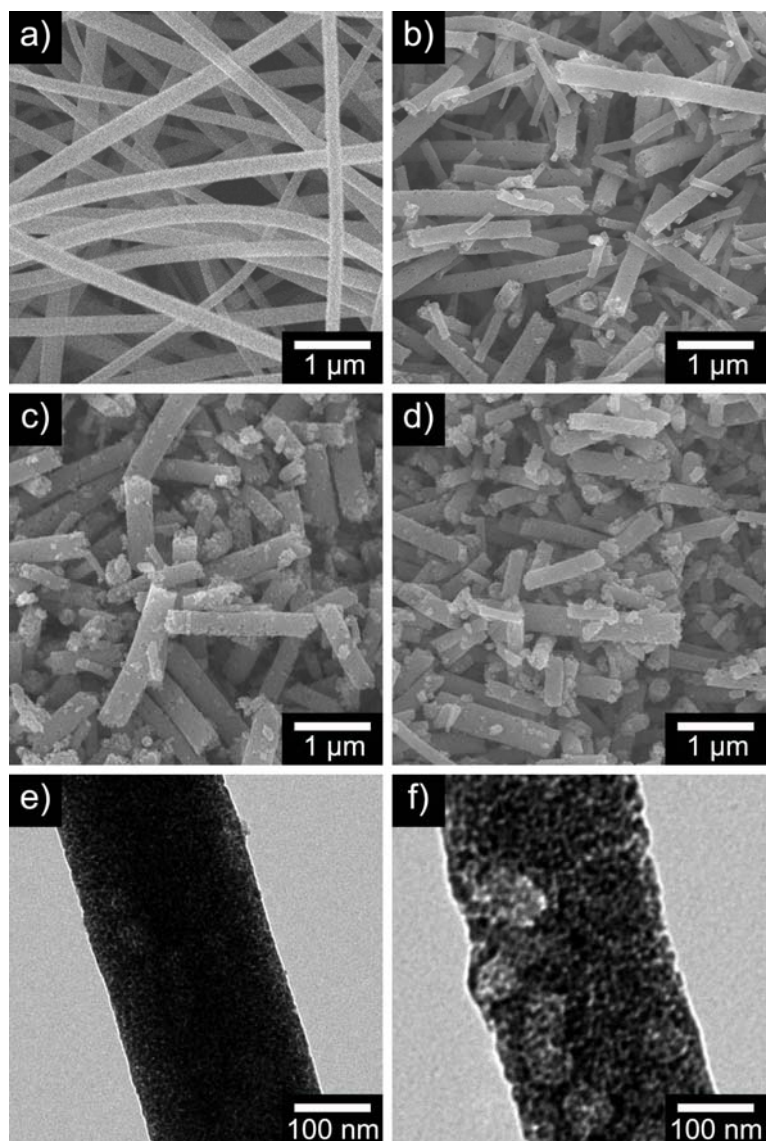


Figure 2. FE-SEM images of a) $\text{SiO}_2/\text{TiO}_2$ composite NFs and porous TiO_2 NFs b) TEOS 1 %, c) TEOS 1.5 %, d) TEOS 2 %. TEM images of e) $\text{SiO}_2/\text{TiO}_2$ composite NF and f) porous TiO_2 NF.

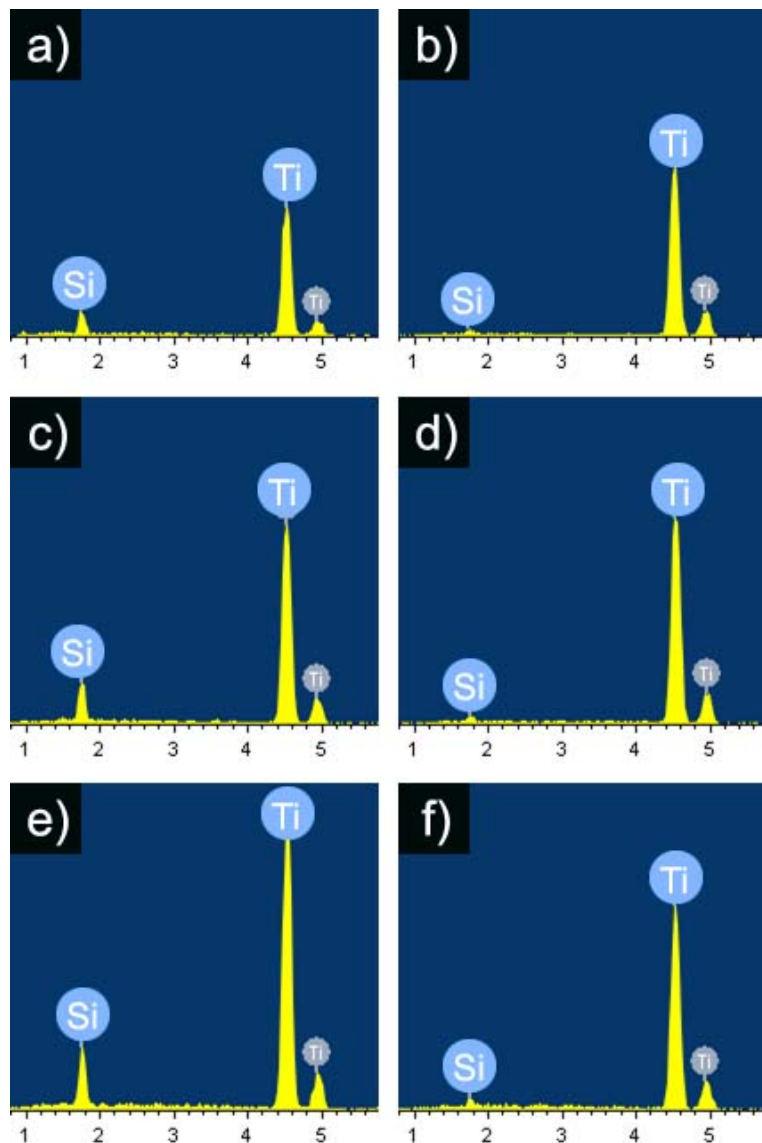


Figure 3. SEM/energy dispersive X-ray spectroscopy (SEM/EDX) spectra SiO₂/TiO₂ composite NFs (before etching) a) TEOS 1 %, c) TEOS 1.5 %, e) TEOS 2 % and porous TiO₂ NFs (after etching) b) TEOS 1 %, d) TEOS 1.5 %, f) TEOS 2 %.

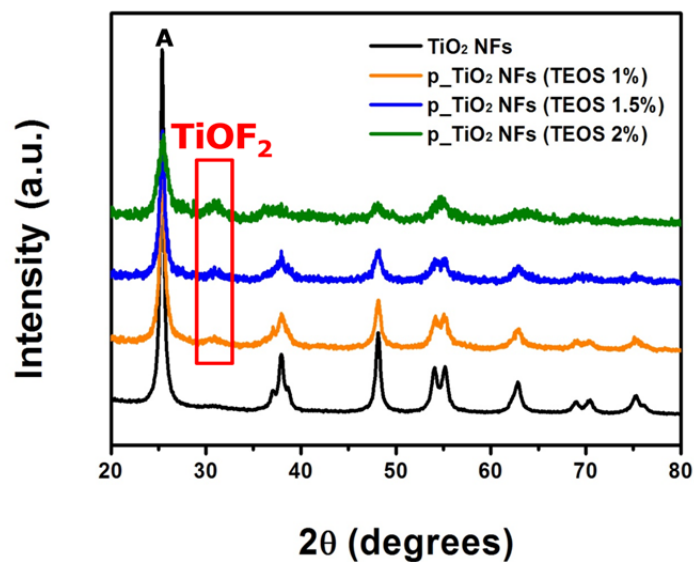


Figure 4. XRD patterns for pure TiO_2 NFs (black) and porous TiO_2 NFs with TEOS 1 % (yellow), TEOS 1.5 % (blue), TEOS 2 % (green). The letter “A” denotes peaks for the anatase phase.

3.1.3 Surface area analysis of porous TiO₂ NFs

Analysis of nitrogen adsorption isotherm used to measure the specific surface area of porous TiO₂ NFs. All the isotherms of the porous TiO₂ NFs showed the hysteresis loops corresponding to type IV behavior. Brunauer-Emmett-Teller (BET) analysis presents that porous TiO₂ NFs had higher surface area than pure TiO₂ NFs as shown in **Figure 5** and **Table 1**. For porous TiO₂ NFs (TEOS 1%), porous TiO₂ NFs (TEOS 1.5%) and porous TiO₂ NFs (TEOS 2%), the BET surface areas were 95, 117 and 163 m² g⁻¹, which are tremendously enhanced values compared with the surface area of pure TiO₂ NFs (19 m² g⁻¹).

The absorption spectrum of N719 desorbed from TiO₂ NFs films in NaOH mixed solution exhibit that the dye loading is significantly increasing between pure TiO₂ NFs and porous TiO₂ NFs (**Figure 6**).

The amounts of dye loading on TiO₂ NFs films shown in the scond

column of **Table 1**. Considering surface area analysis data (**Figure 5, Table 1**) in connection with dye-loading experiments (**Figure 6, Table 1**), it confirmed that porous TiO₂ NFs offer a larger surface area on which dye molecules adsorb than pure TiO₂ NFs. As indicated in **Table 1**, amount of dye on TiO₂ NFs depends on surface area with increasing TEOS content from 0 to 1.5 %. However, porous TiO₂ NFs (TEOS 2%) shows decreased value of dye adsorption whereas they have largest surface area of all samples. Judging from the XRD data, TiOF₂ is formed more with increasing TEOS amount, leading to decrease of dye binding site on TiO₂ surface.

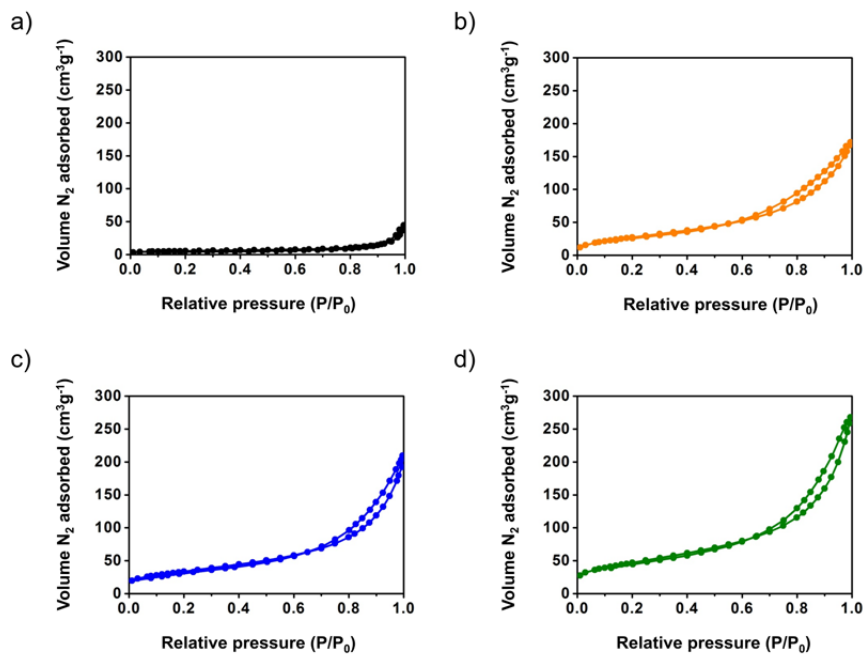


Figure 5. Nitrogen adsorption isotherms of a) pure TiO₂ NFs and porous TiO₂ NFs b) TEOS 1 %, c) TEOS 1.5 %, d) TEOS 2 %.

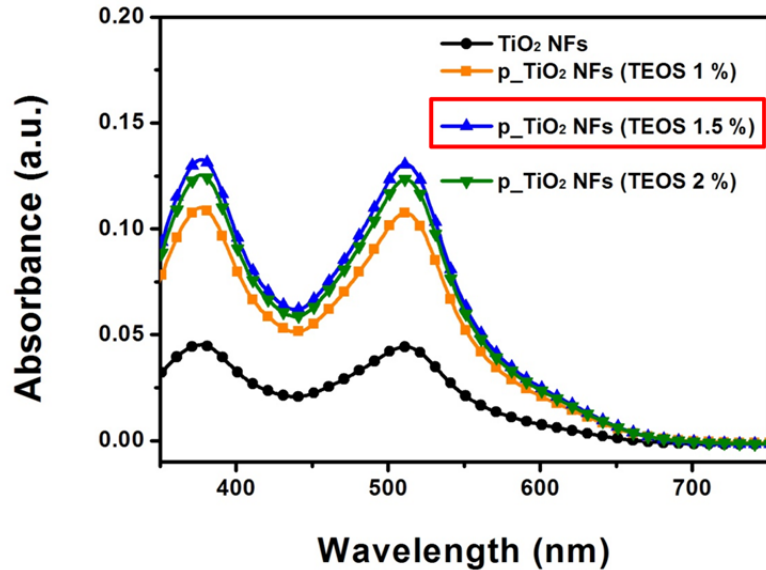


Figure 6. Absorption spectra of N719 in NaOH mixed solution
 (water/ethanol = 1:1, v/v) desorbed from photoelectrode based on pure
 TiO₂ NFs (black) and porous TiO₂ NFs with TEOS 1 % (yellow),
 TEOS 1.5 % (blue), TEOS 2 % (green).

Table 1. BET surface area and dye loading amount of pure TiO₂ NFs and porous TiO₂ NFs with increasing TEOS content.

Sample	BET Surface area (m ² g ⁻¹)	Dye loading (×10 ⁷ mol cm ⁻²)
TiO ₂ NFs	19	0.62
p_TiO ₂ NFs (TEOS 1 %)	95	1.51
p_TiO ₂ NFs (TEOS 1.5 %)	117	1.84
p_TiO ₂ NFs (TEOS 2 %)	163	1.74

3.1.4 Solar cell performance

Figure 7 illustrates the photocurrent density-voltage characteristics of DSSCs prepared with pure TiO₂ NFs and porous TiO₂ NFs. The corresponding values of these photovoltaic parameters, such as the short-circuit photocurrent density (J_{sc}), open-circuit voltage (V_{oc}), fill factor (FF), and power conversion efficiency (PCE, η), are presented in **Table 2**. The PCE of DSSCs fabricated from porous TiO₂ NFs (TEOS 1 %), porous TiO₂ NFs (TEOS 1.5 %) and porous TiO₂ NFs (TEOS 2%) were 7.6, 7.9 and 7.6 %, which are comparable to that of pure TiO₂ NFs (6.2 %). Superior dye-loading amount with high surface area play a key role in improving J_{sc} , leading to achieving a high performance DSSC. J_{sc} of DSSCs increased in order of porous TiO₂ NFs (TEOS 1 %) < porous TiO₂ NFs (TEOS 2%) < porous TiO₂ NFs (TEOS 1.5 %), resulting in a similar variation tendency to the corresponding PCE of DSSCs. The

J_{sc} and efficiency variation trends are also the same as dye loading amount trend. The results indicate that porous TiO₂ NFs (TEOS 1.5%) has the optimization because they have higher binding site for the attachment of dye molecules on TiO₂ surface than others.

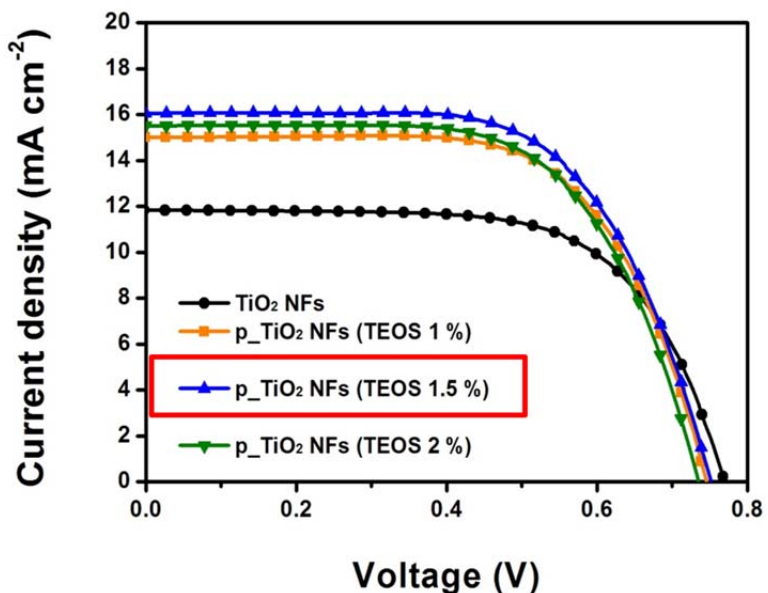


Figure 7. *J-V* characteristics of DSSCs prepared with pure TiO₂ NFs (black) and porous TiO₂ NFs with TEOS 1 % (yellow), TEOS 1.5 % (blue), TEOS 2 % (green)..

Table 2. Summary of the J - V characteristics of DSSCs prepared with various surface areas.

Sample	J_{sc} (mA cm $^{-2}$)	V_{oc} (V)	FF	η (%)
TiO ₂ NFs	11.8	0.78	0.67	6.2
p-TiO ₂ NFs (TEOS 1 %)	15.1	0.76	0.67	7.6
p-TiO ₂ NFs (TEOS 1.5 %)	16.1	0.76	0.65	7.9
p-TiO ₂ NFs (TEOS 2 %)	15.6	0.75	0.65	7.6

3.2 Ag NPs decorated porous TiO₂ NFs for solar cell application

3.2.1 Mechanism of Ag NPs in reduction process

The reduction of Ag NPs proceeded on the MPTS-treated porous TiO₂ NFs. The MPTS-treated porous TiO₂ NFs is partially negative because their surface has the thiol group [47]. The silver ions preferentially attached to the MPTS-treated porous TiO₂ NFs due to charge–charge interactions between the cationic silver ions and the negatively charged MPTS-treated porous TiO₂ NFs surface. Octylamine induced the reduction of silver ions during the reaction [48]. After nucleation and growth process, Ag NPs are formed on the porous TiO₂ NFs.

3.2.2 Characterization of Ag NPs decorated porous TiO₂ NFs

The TEM image shown in **Figure 8** confirms that silver nanoparticles on porous TiO₂ NFs were synthesized with an average diameter of 25 nm. In TEM image, it is clear that Ag NPs decorated porous TiO₂ NFs is coated with a uniform and thin SiO₂ shell and the average shell thickness of SiO₂ is about 5 nm. The data represents that the protecting layer of Ag NPs was successfully formed.

To understand the atomic distribution, scanning transmission electron microscopy/energy dispersive X-ray (STEM-EDX) dot mapping was performed. In **Figure 9**, the images indicated that the NFs consisted of titanium (green), silicon (sky blue), silver (purple), and oxygen (yellow). Mapping result clearly revealed that Ag NPs were well distributed on the porous TiO₂ NFs. Orange region represented silica domains with slightly larger diameter than green

region represented titania core located on inner part of NFs.

Therefore, from this observation, it was proved that the SiO₂ protecting shell was perfectly synthesized.

XRD analysis (**Figure 10**) confirmed the crystallinity of porous TiO₂ NFs (black) and Ag NPs decorated porous TiO₂ NFs (red).

XRD pattern of Ag NPs decorated porous TiO₂ NFs confirms that it is comprised of the peaks of TiO₂ anatase phase and Ag crystalline phase. The peak centered at $2\theta = 38.0^\circ$ implied the existence of crystalline Ag and the strong diffraction peak at $2\theta = 25.3^\circ$ well in good agreement with the peak for anatase TiO₂ [49].

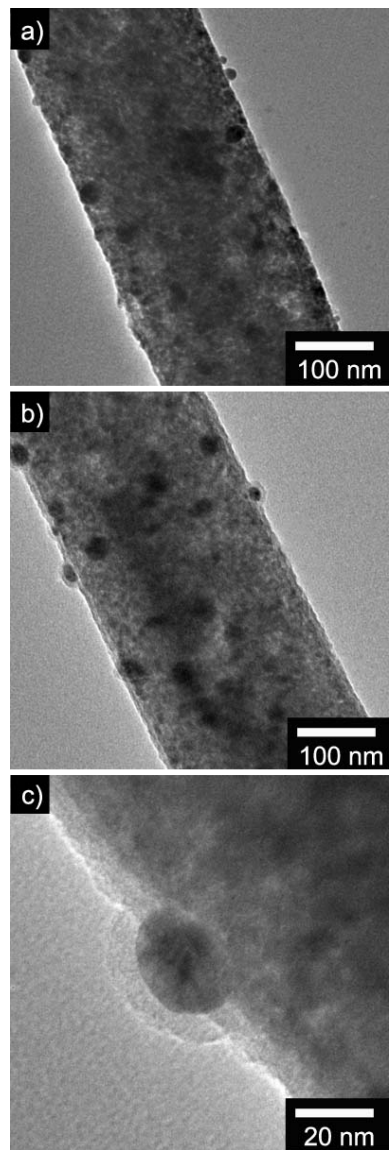


Figure 8. TEM images of a) Ag/p_{_}TiO₂ NFs and b), c) Ag/p_{_}TiO₂ NFs with SiO₂ protecting layer.

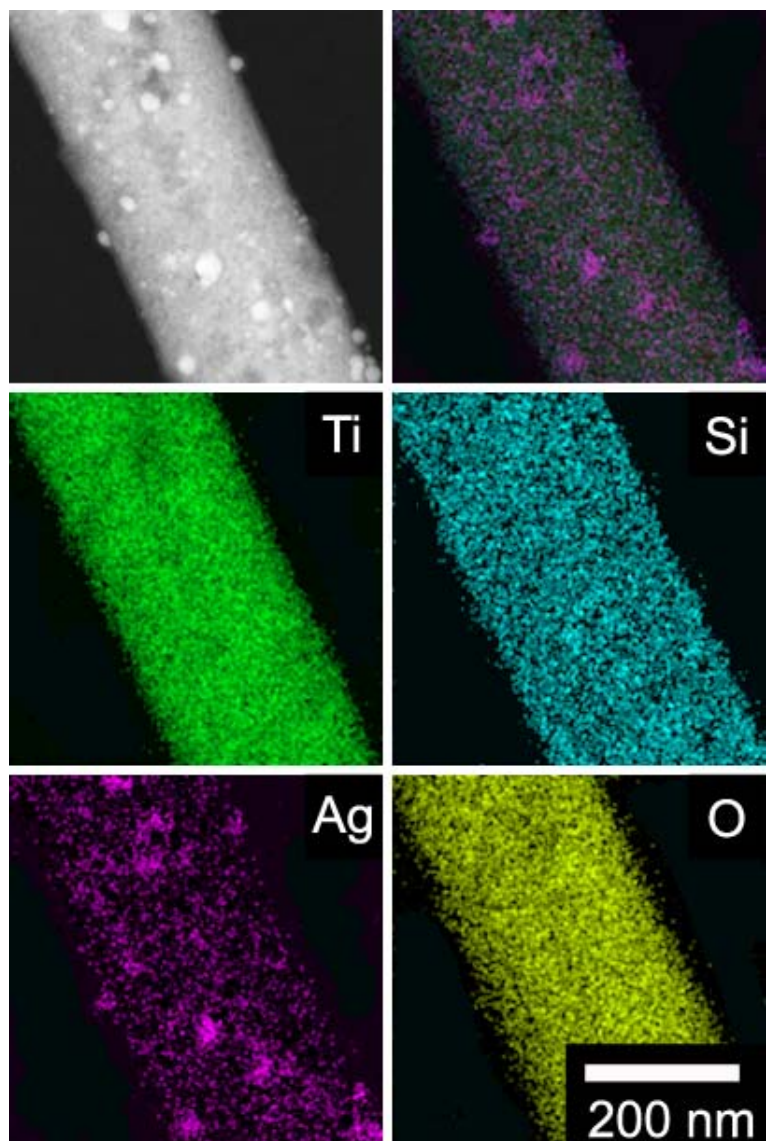


Figure 9. Scanning transmission electron microscopy/energy dispersive X-ray (STEM-EDX) dot mapping of Ag/p_{_}TiO₂ NFs with SiO₂ protecting layer.

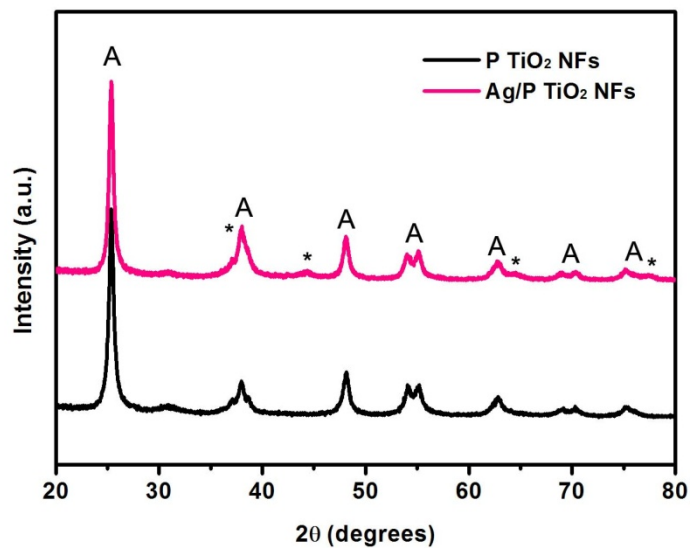


Figure 10. XRD patterns for a) porous TiO₂ NFs and b) Ag/p-TiO₂ NFs. The letter “A” denotes peaks for the anatase phase and * denotes peaks for silver.

3.2.3 Optical property analysis

To gain some insight into the light induced effects by Ag NPs, the optical absorption of porous TiO₂ NFs and Ag NPs decorated porous TiO₂ NFs suspensions in ethanol was investigated. **Figure 11b** shows the absorbance difference between Ag/p-TiO₂ NFs and p-TiO₂ NFs. The enhanced optical absorption around 450 nm is attributed to the surface plasmon effect introduced by Ag NPs [50].

To verify the effect of surface plasmons from Ag NPs on the absorbance of ruthenium dye, we subjected ruthenium dye, porous TiO₂ NFs with dye and Ag/p-TiO₂ NFs with dye in ethanol to UV irradiation. Under our experimental condition, dye has two maximum peak positions at 390, 530 nm corresponded to metal-ligand charge-transfer (MLCT) transition (**Figure 12**) [51]. In order to achieve an in-depth insight into the surface plasmon effect on light absorption of dye, the light absorbance of NFs (**Figure 11a**)

has been excluded from the light absorbance of NFs with dye (**Figure 12a**). Absorbance results from only dye are calculated in the following manner: (absorbance of NFs with dye(λ)) - (absorbance of NFs(λ)) and the concentrations of NFs and dyes in ethanol are exactly same. The light absorption of only dye with the presence of Ag/p_xTiO₂ NFs shows enhanced values comparable to the result obtained with the presence of porous TiO₂ NFs. As discussed previously reported observations on plasmon-enhanced dye absorption, the increase of absorbance of dye is due to the interaction of the dye molecular dipole and enhanced electromagnetic field occurring near the Ag nanoparticle surface, if the light wavelength resonates with the surface plasmon frequency [42] [52].

The absorption spectrum of N719 desorbed from p_xTiO₂ NFs and Ag/p_xTiO₂ NFs films in NaOH mixed solution shown in **Figure 13**.

The dye loading obtained for Ag/p_xTiO₂ NFs with various content of Ag was almost the same as that for p-TiO₂ NFs. It is confirmed that dye loading amount is completely unrelated with Ag percent of photoelectrode.

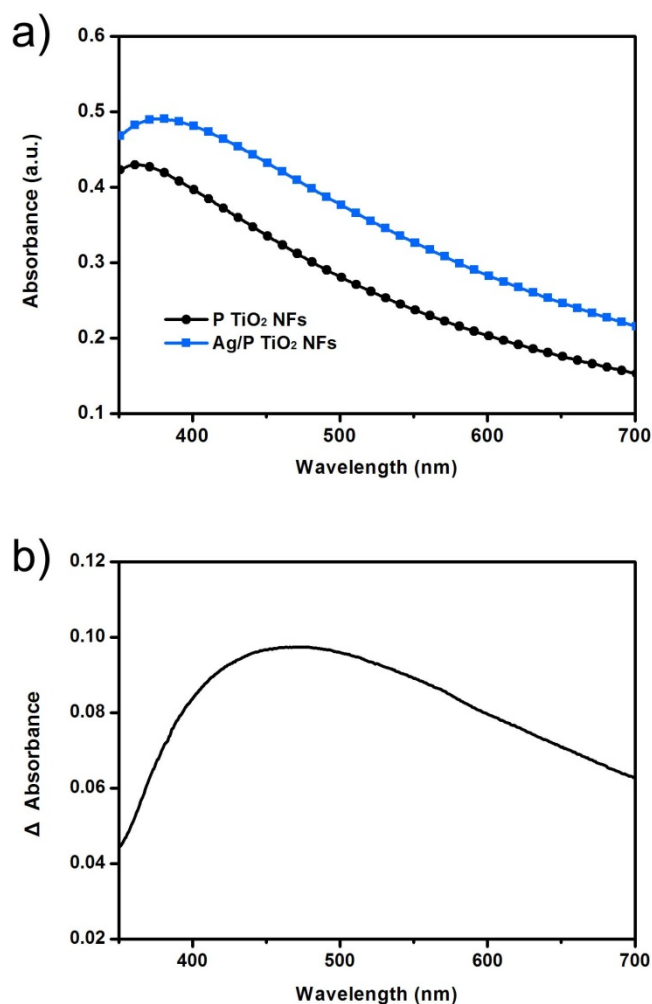


Figure 11. a) Optical absorption spectra of porous TiO₂ NFs (black) and Ag/p_TiO₂ NFs (blue) in ethanol and b) difference of optical absorbance.

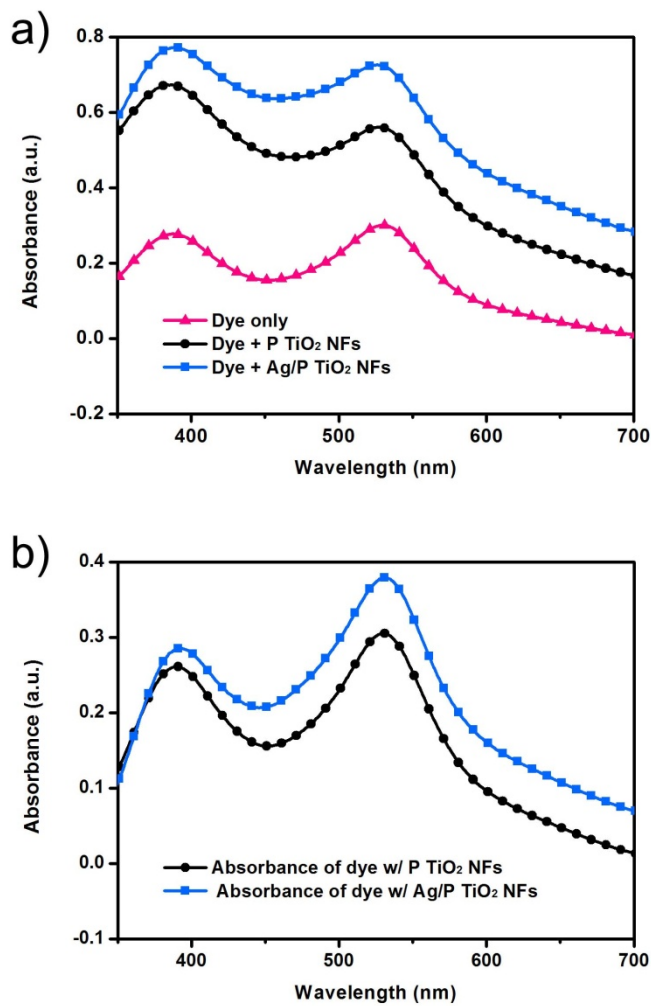


Figure 12. a) Optical absorption spectra of ruthenium dye molecules (red), p-TiO₂ NFs with dye (black) and Ag/p-TiO₂ NFs with dye (blue) in ethanol. b) Absorbance results from only dye are calculated in the following manner: (absorbance of NFs with dye(λ)) - (absorbance of NFs(λ)).

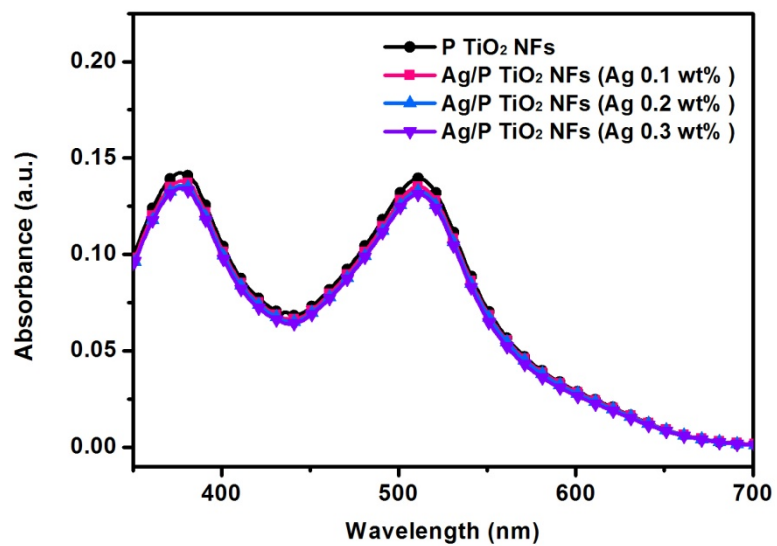


Figure 13. Absorption spectra of N719 in NaOH mixed solution
(water/ethanol = 1:1, v/v) desorbed from photoelectrode based on
porous TiO₂ NFs (black) and Ag NPs decorated porous TiO₂ NFs with
Ag 0.1wt % (red), Ag 0.2wt % (blue), Ag 0.3wt % (violet).

3.2.4 Solar cell performance

To investigate the effect of surface plasmons on device performance, we compared the performance of DSSCs prepared with porous TiO₂ NFs and Ag NPs decorated porous TiO₂ NFs. The power conversion efficiencies were measured with 0.1, 0.2, 0.3 wt% of Ag NPs to optimize the device performance. The photocurrent density-voltage curves of DSSCs are shown in **Figure 14** and the short-circuit photocurrent density (J_{sc}), open-circuit voltage (V_{oc}), fill factor (FF), and power conversion efficiency (PCE, η), are collected in **Table 3**. The porous TiO₂ NFs-based DSSC showed a PCE of 7.9 %, whereas the plasmon-enhanced DSSC made with 0.2 wt% Ag NPs had the highest PCE of 8.8%. Compared with the porous TiO₂ NFs-based DSSC, the open-circuit voltage and fill factor of the DSSCs containing Ag NPs were similar, while the short-circuit photocurrent density significantly increased from 16.1

to 17, 18.2, 17.5 mA cm⁻². The improved photocurrent density in the DSSCs containing Ag NPs is attributed to the strongly localized electromagnetic field around the Ag NPs, leading to the increased optical absorption efficiency of dye molecules. The decrease of J_{sc} and PCE was observed in the plasmon-enhanced DSSC made with 0.3 wt% Ag NPs. It is considered that excess Ag NPs trapped the photogenerated electrons and transformed the part of absorbed incident light into heat [52].

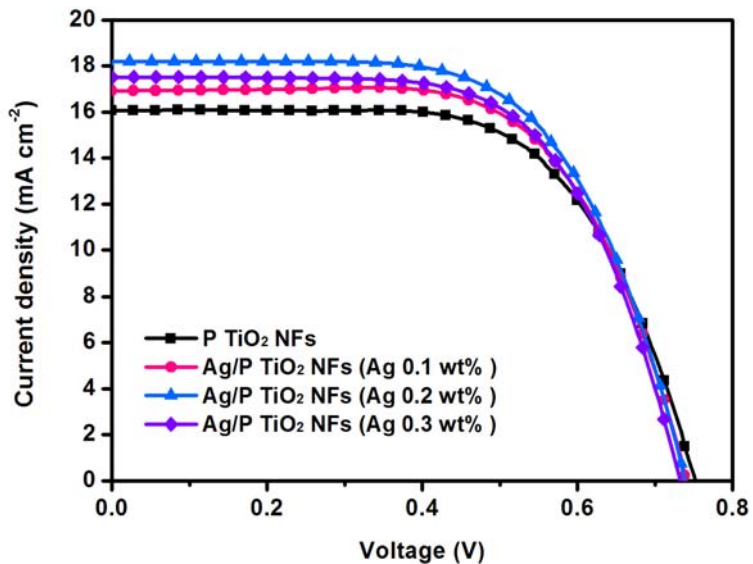


Figure 14. J - V characteristics of DSSCs prepared with porous TiO_2 NFs (black) and Ag NPs decorated porous TiO_2 NFs with Ag 0.1wt % (red), Ag 0.2wt % (blue), Ag 0.3wt % (violet).

Table 3. Summary of the J - V characteristics of DSSCs prepared with different ratio of silver nanoparticles.

Sample	J_{sc} (mA cm $^{-2}$)	V_{oc} (V)	FF	η (%)
p_ TiO ₂ NFs	16.1	0.76	0.65	7.9
Ag/p_ TiO ₂ NFs (Ag 0.1wt%)	17.0	0.75	0.66	8.3
Ag/p_ TiO ₂ NFs (Ag 0.2 wt%)	18.2	0.75	0.65	8.8
Ag/p_ TiO ₂ NFs (Ag 0.3 wt%)	17.5	0.74	0.66	8.5

Chapter 4. Conclusion

In conclusion, porous TiO₂ NFs with various surface areas and silver NPs decorated porous TiO₂ NFs were successfully fabricated. High surface areas of porous TiO₂ NFs can provide sufficient adsorption of sensitizers on TiO₂ NFs surface for enhanced light harvesting result in increase photocurrent. Moreover, Ag NPs decorated porous TiO₂ NFs exhibited the greatest light absorption and photocurrent because of a surface plasmon effect of Ag NPs. The DSSC using Ag NPs decorated porous TiO₂ NFs showed an increased current density and ca. 42% enhanced power conversion efficiency compared to the pristine TiO₂ nanofibers-based DSSC. Furthermore, it is anticipated that the Ag NPs decorated porous TiO₂ NFs can be used in various applications in the photocatalyst and solar cell fields.

References

1. B. O'Regan and M. Graetzel, *Nature*, **1991**, *353*, 737.
2. M. Dürr, A. Schmid, M. Obermaier, S. Rosselli, A. Yasuda and G. Nelles, *Nature Materials*, **2005**, *4*, 607-611.
3. M. Grätzel, *Nature*, **2001**, *414*, 338-344.
4. B. E. Hardin, H. J. Snaith and M. D. McGehee, *Nature Photonics*, **2012**, *6*, 162-169.
5. A. Hagfeldt, G. Boschloo, L. Sun, L. Kloo and H. Pettersson, *Chemical Reviews*, **2010**, *110*, 6595-6663.
6. N. Papageorgiou, W. F. Maier and M. Grätzel, *Journal of the Electrochemical Society*, **1997**, *144*, 876-884.
7. A. Yella, H. W. Lee, H. N. Tsao, C. Yi, A. K. Chandiran, M. K. Nazeeruddin, E. W. G. Diau, C. Y. Yeh, S. M. Zakeeruddin and M. Grätzel, *Science*, **2011**, *334*, 629-634.
8. A. Mishra, M. K. R. Fischer and P. Büuerle, *Angewandte Chemie - International Edition*, **2009**, *48*, 2474-2499.
9. B. Liu and E. S. Aydil, *Journal of the American Chemical Society*, **2009**, *131*, 3985-3990.
10. S. Son, S. H. Hwang, C. Kim, J. Y. Yun and J. Jang, *ACS applied materials & interfaces*, **2013**.
11. J. Jang, J. Bae, M. Choi and S. H. Yoon, *Carbon*, **2005**, *43*,

2730-2736.

12. F. Di Benedetto, A. Camposeo, S. Pagliara, E. Mele, L. Persano, R. Stabile, R. Cingolani and D. Pisignano, *Nature Nanotechnology*, **2008**, *3*, 614-619.
13. S. J. Park, O. S. Kwon and J. Jang, *Chemical Communications*, **2013**, *49*, 4673-4675.
14. Y. Xia, P. Yang, Y. Sun, Y. Wu, B. Mayers, B. Gates, Y. Yin, F. Kim and H. Yan, *Advanced Materials*, **2003**, *15*, 353-389.
15. D. Li and Y. Xia, *Advanced Materials*, **2004**, *16*, 1151-1170.
16. X. Lu, C. Wang and Y. Wei, *Small*, **2009**, *5*, 2349-2370.
17. X. P. Lin, D. M. Song, X. Q. Gu, Y. L. Zhao and Y. H. Qiang, *Applied Surface Science*, **2012**, *263*, 816-820.
18. V. Ganapathy, B. Karunagaran and S. W. Rhee, *Journal of Power Sources*, **2010**, *195*, 5138-5143.
19. Y.-L. Xie, Z.-X. Li, Z.-G. Xu and H.-L. Zhang, *Electrochemistry Communications*, **2011**, *13*, 788-791.
20. M. Y. Song, D. K. Kim, S. M. Jo and D. Y. Kim, *Synthetic Metals*, **2005**, *155*, 635-638.
21. S. H. Hwang, C. Kim, H. Song, S. Son and J. Jang, *ACS applied materials & interfaces*, **2012**, *4*, 5287-5292.
22. J. Qu, G. R. Li and X. P. Gao, *Energy & Environmental Science*, **2010**, *3*, 2003.

23. M. Wang, Y. Wang and J. Li, *Chem Commun (Camb)*, **2011**, *47*, 11246-11248.
24. G. Pfaff and P. Reynders, *Chemical Reviews*, **1999**, *99*, 1963-1981.
25. S. H. Hwang, C. Kim and J. Jang, *Catalysis Communications*, **2011**, *12*, 1037-1041.
26. U. Bach, D. Lupo, P. Comte, J. E. Moser, F. Weissortel, J. Salbeck, H. Spreitzer and M. Grätzel, *Nature*, **1998**, *395*, 583-585.
27. X. Chen and S. S. Mao, *Chemical Reviews*, **2007**, *107*, 2891-2959.
28. L. Yang and W. W. F. Leung, *Advanced Materials*, **2011**, *23*, 4559-4562.
29. B. H. Lee, M. Y. Song, S. Y. Jang, S. M. Jo, S. Y. Kwak and D. Y. Kim, *Journal of Physical Chemistry C*, **2009**, *113*, 21453-21457.
30. S. Chuangchote, T. Sagawa and S. Yoshikawa, *Applied Physics Letters*, **2008**, *93*.
31. G. Schmid, *Nanoparticles*, Wiley-VCH, 2004.
32. C. P. Poole, *Introduction to nanotechnology*, Wiley-VCH, 2003.
33. H. Yoon, M. Choi, K. J. Lee and J. Jang, *Macromolecular Research*, **2008**, *16*, 85-102.

34. J. Jang, *Advances in Polymer Science* **2006**, *199*, 189-259.
35. Y. Volokitin, J. Sinzig, L. J. De Jongh, G. Schmidt, M. N. Vargaftik and I. I. Moiseev, *Nature*, **1996**, *384*, 621-623.
36. K. Watanabe, D. Menzel, N. Nilius and H. J. Freund, *Chemical Reviews*, **2006**, *106*, 4301-4320.
37. K. L. Kelly, E. Coronado, L. L. Zhao and G. C. Schatz, *Journal of Physical Chemistry B*, **2003**, *107*, 668-677.
38. M. Pelton, J. Aizpurua and G. Bryant, *Laser & Photonics Review*, **2008**, *2*, 136-159.
39. H. Tan, R. Santbergen, A. H. Smets and M. Zeman, *Nano letters*, **2012**, *12*, 4070-4076.
40. K. R. Catchpole and A. Polman, *Optics Express*, **2008**, *16*, 21793-21800.
41. I. K. Ding, J. Zhu, W. Cai, S. J. Moon, N. Cai, P. Wang, S. M. Zakeeruddin, M. Grätzel, M. L. Brongersma, Y. Cui and M. D. McGehee, *Advanced Energy Materials*, **2011**, *1*, 52-57.
42. M. Ihara, K. Tanaka, K. Sakaki, I. Honma and K. Yamada, *Journal of Physical Chemistry B*, **1997**, *101*, 5153-5157.
43. M. Rycenga, C. M. Cobley, J. Zeng, W. Li, C. H. Moran, Q. Zhang, D. Qin and Y. Xia, *Chem Rev*, **2011**, *111*, 3669-3712.
44. W. Stöber, A. Fink and E. Bohn, *Journal of Colloid And Interface Science*, **1968**, *26*, 62-69.
45. T. Hoshino and Y. Nishioka, *Journal of Chemical Physics*,

1999, *III*, 2109-2114.

46. J. Zhu, D. Zhang, Z. Bian, G. Li, Y. Huo, Y. Lu and H. Li, *Chemical Communications*, **2009**, 5394-5396.
47. J. H. Kim, J. S. Kim, H. Choi, S. M. Lee, B. H. Jun, K. N. Yu, E. Kuk, Y. K. Kim, D. H. Jeong, M. H. Cho and Y. S. Lee, *Analytical Chemistry*, **2006**, 78, 6967-6973.
48. H. Kang, T. Kang, S. Kim, J.-H. Kim, B.-H. Jun, J. Chae, J. Park, D.-H. Jeong and Y.-S. Lee, *Journal of Nanoscience and Nanotechnology*, **2011**, *II*, 579-583.
49. Y. Sun, Y. Yin, B. T. Mayers, T. Herricks and Y. Xia, *Chemistry of Materials*, **2002**, *14*, 4736-4745.
50. L. W. Jang, D. W. Jeon, M. Kim, J. W. Jeon, A. Y. Polyakov, J. W. Ju, S. J. Lee, J. H. Baek, J. K. Yang and I. H. Lee, *Advanced Functional Materials*, **2012**, *22*, 2728-2734.
51. N. C. Jeong, C. Prasittichai and J. T. Hupp, *Langmuir*, **2011**, *27*, 14609-14614.
52. J. Qi, X. Dang, P. T. Hammond and A. M. Belcher, *ACS Nano*, **2011**, *5*, 7108-7116.

초 록

은 나노입자가 부착된 다공성 이산화티타늄 나노섬유를 제조하였고 이를 고효율 염료감응태양전지에 응용하였다. 이산화티타늄/이산화규소 혼합나노섬유를 전기방사로 제조한 뒤 이산화규소 부분을 불산으로 식각 시켜 다공성이산화티타늄 나노섬유의 표면적을 조절하였다. 높은 표면적을 지니게 된 다공성 이산화티타늄 나노섬유의 경우, 이산화티타늄 표면에 부착되는 염료의 양이 증가하는 것을 확인하였다. 다공성 이산화티타늄 나노섬유 표면에 부착된 은 나노입자의 표면 플라스몬 효과는 입사광의 흡광 및 산란을 증가시킬 뿐만 아니라 염료에 의해 흡수되는 광량의 증가를 유도하는 것을 확인하였다. 그 결과, 은 나노입자가 부착 된 다공성 이산화티타늄 나노섬유를 염료감응태양전지의 음극물질로 적용하였을 때, 이산화티타늄 나노섬유로 이루어진 전지의 효율인 6.2 %에 비하여 8.8 %로 최적화된 효율을 보였다.

주요어: 염료감응태양전지, 이산화티타늄 나노섬유, 은 나노입자,

표면 플라스몬

학번: 2011-24097